THE JOURNAL OF PHYSICAL CHEMISTRY B

Article

pubs.acs.org/JPCB

Concentrating and Recycling Energy in Lanthanide Codopants for Efficient and Spectrally Pure Emission: The Case of $NaYF_4$:Er^{3+}/Tm^{3+} Upconverting Nanocrystals

Emory M. Chan,* Daniel J. Gargas, P. James Schuck, and Delia J. Milliron

The Molecular Foundry, Lawrence Berkeley National Laboratory, Berkeley, California 94720, United States

Supporting Information

ABSTRACT: In lanthanide-doped materials, energy transfer (ET) between codopant ions can populate or depopulate excited states, giving rise to spectrally pure luminescence that is valuable for the multicolor imaging and simultaneous tracking of multiple biological species. Here, we use the case study of $NaYF_4$ nanocrystals codoped with Er^{3+} and Tm^{3+} to theoretically investigate the ET mechanisms that selectively enhance and suppress visible upconversion luminescence under near-infrared excitation. Using an experimentally validated population balance model and using a path-tracing algorithm to objectively identify transitions with the most significant contributions, we isolated a network of six pathways that combine to divert energy away from the green-emitting manifolds and concentrate it in the Tm^{3+}:$^3F_4$ manifold, which then participates in energy transfer upconversion (ETU) to populate the red-emitting Er^{3+}:$^4F_{9/2}$ manifold. We conclude that the strength of this ETU process is a function of the strong coupling of the Tm^{3+}:$^3F_4$ manifold and its ground state, the near-optimum band alignment of Er^{3+} and Tm^{3+} manifolds, and the concentration of population in Tm^{3+}:$^3F_4$. These factors, along with the ability to recycle energy not utilized for red emission, also contribute to the enhanced quantum yield of $NaYF_4$:Er^{3+}/Tm^{3+}. We generalize a scheme for applying these energy concentration and recycling pathways to other combinations of lanthanide dopants. Ultimately, these ET pathways and others elucidated by our theoretical modeling will enable the programming of physical properties in lanthanide-doped materials for a variety of applications that demand strong and precisely defined optical transitions.

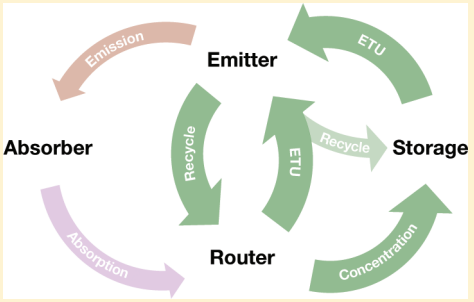

INTRODUCTION

Energy transfer (ET) is an indispensable tool for investigating biological and molecular processes, enabling sensitive and selective assays,[1] the measurement of intermolecular distances,[2] and the simultaneous fluorescent detection of multiple species using a single excitation source.[3] Recently, energy transfer upconversion (ETU)[4] has enabled the visible-spectrum imaging of lanthanide-doped nanocrystal phosphors[5] excited with near-infrared (NIR) radiation.[6,7] Because upconverting nanoparticles (UCNPs) each contain hundreds of dopants embedded in an inert matrix, e.g., $NaYF_4$,[8] upconverting probes exhibit exceptionally stable luminescence,[9,10] do not photobleach,[11] and are biocompatible.[12] The long lifetimes of lanthanide excited states promote efficient excited state absorption (ESA) and ETU,[13,14] allowing the prolonged imaging of cells and internal organs[15,16] with NIR radiation, which reduces photodamage, autofluorescence, and scattering.[5,6] However, the dense and diverse lanthanide $4f^N$ electronic structures[17] that promote upconversion (UC) also give rise to emission spectra containing multiple peaks[18] that can hinder the independent and simultaneous imaging of multiple species.[18,19]

In this work, we use the case study of $NaYF_4$ nanoparticles codoped with Er^{3+} and Tm^{3+} to theoretically investigate the mechanisms through which energy transfer between dopants selectively promotes or suppresses specific lanthanide upconverted luminescence wavelengths. In a recent combinatorial survey, we identified the Er^{3+}/Tm^{3+} combination, with its singular red emission at 660 nm (Er^{3+}:$^4F_{9/2} \rightarrow {}^4I_{15/2}$), as having the most spectrally pure upconverted emission out of all binary combinations of lanthanide ions excited at 980 nm wavelength. Unlike other color tuning strategies with which emission intensities decrease with higher spectral purity,[20−23] the addition of Tm^{3+} to Er^{3+}-doped materials enhances intensities by 2 to 60 times while simultaneously enhancing spectral purity.[24−26]

Previous reports[24−27] have noted the preferential red emission of Er^{3+}/Tm^{3+}-doped bulk materials and have proposed ET mechanisms consistent with observations. However, evidence for proposed ET pathways is indirect and does not exclude alternate mechanisms, due to the experimental difficulty of mapping energy transfer processes between dopant excited states. Furthermore, the photophysics and ET of the Er^{3+}/Tm^{3+} couple have not been studied in colloidal nanocrystals, which often exhibit size-dependent physical properties.[28]

Special Issue: Richard A. Mathies Festschrift

Received: March 12, 2012
Revised: April 26, 2012

   dx.doi.org/10.1021/jp302401j | J. Phys. Chem. B XXXX, XXX, XXX−XXX

Here, we investigate and quantify the contributions of the ET processes that populate and depopulate the excited states responsible for spectrally pure emission in Er^{3+}/Tm^{3+}-doped materials. To isolate the critical ET pathways, we developed a comprehensive theoretical model that accounts for all possible absorption, radiative, nonradiative, and energy transfer processes among the dopants without assuming a given mechanism. We validated this model thoroughly by comparing simulated transition rates with experimental high-throughput screening data. Quantitative simulation data, such as branching and contribution fractions, enabled us to trace the major and minor pathways leading to visible luminescence. From these, we conclude that the spectral purity and the efficiency of red emission in the Er^{3+}/Tm^{3+} combination are a result of a series of ET processes in which energy is concentrated in the lowest-lying Tm^{3+} excited state, which can then promote ETU to the red-emitting Er^{3+} manifold. For alternate pathways, energy is recycled and directed back into major pathways, minimizing energy loss. These energy concentration and recycling mechanisms are applicable to other combinations of lanthanide dopants, which can be predicted with our theoretical model. Such efficient and spectrally pure upconverting nanomaterials will be essential for prolonged imaging and tracking of multiple species in a variety of environments.

Theory. Since the intensity of a given radiative transition is proportional to the product of the population of the emitting state and the microscopic rate constant for the transition, we used a set of coupled differential equations to describe the instantaneous populations of the Er^{3+} and Tm^{3+} manifolds. In this population balance model, the population N_i (in nm^{-3}) of a lanthanide $4f^N$ manifold i over time is determined by the incoming and outgoing rates of electric dipole (ED)[29] and magnetic dipole (MD)[29,30] radiative transitions, nonradiative multiphonon relaxation (MPR),[31,32] and energy transfer (ET),[33,34] as shown in eq 1

$$\frac{dN_i}{dt} = \sum_j (N_j A_{ji}^{ED} - N_i A_{ij}^{ED}) + \sum_j (N_j A_{ji}^{MD} - N_i A_{ij}^{MD}) + (N_{i+1} W_{i+1,i}^{NR} - N_i W_{i,i-1}^{NR}) + \sum_{ij,kl} (N_j N_l P_{ji,lk}^{ET} - N_i N_k P_{ij,kl}^{ET}) \quad (1)$$

A_{ij}^{ED} and A_{ij}^{MD} (s^{-1}) are the Einstein coefficients for ED and MD radiative transitions from manifold i to j. $W_{i,i-1}^{NR}$ (s^{-1}) is the nonradiative MPR rate from the manifold i to the manifold immediately below i. $P_{ij,kl}^{ET}$ ($nm^3\ s^{-1}$) is the microscopic energy transfer parameter for the transfer of energy for the donor i to j transition and the acceptor k to l transition.

Since each differential equation in eq 1 requires knowledge of rate constants for thousands of i-to-j transitions, it is impractical to determine such constants experimentally for novel materials such as upconverting nanocrystals. Fortunately, several theories allow the calculation of approximate values for these critical parameters. According to Judd–Ofelt theory,[29,35,36] A_{ij}^{ED} can be determined using the reduced matrix elements of the unit tensor operator $U^{(\lambda)}$, $|\langle [SL]J_i \| U^{(\lambda)} \| [SL]J_j \rangle|^2$, in conjunction with three Judd–Ofelt (J–O) parameters, Ω_λ, where λ = 2, 4, or 6

$$A_{ij}^{ED} = \frac{64\pi^4 e^2 \tilde{\nu}^3}{3h(2J+1)} \left[\frac{n(n^2+2)^2}{9} \right] S_{ij}^{ED} \quad (2)$$

$$S_{ij}^{ED} = \sum_{\lambda=2,4,6} \Omega_\lambda |\langle [SL]J_i \| U^{(\lambda)} \| [SL]J_j \rangle|^2 \quad (3)$$

Here, e is the elementary charge; h is Planck's constant; $\tilde{\nu}$ is the energy of the transition in wavenumbers; J is the total angular momentum of the initial state; n is the index of refraction of the material; and S_{ij}^{ED} is the electric dipole line strength, all in the Gaussian unit system. The reduced matrix elements are independent of the host material and can be found in the literature, while the phenomenological Ω_λ parameters are dependent on the material and are fit empirically from absorption spectra.

A_{ij}^{MD} can be calculated with the equation

$$A_{ij}^{MD} = \frac{64\pi^4 e^2 \tilde{\nu}^3}{3h(2J+1)} n^3 S_{ij}^{MD} \quad (4)$$

$$S_{ij}^{MD} = \mu_B{}^2 |\langle [SL]J_i \| \mathbf{L} + 2\mathbf{S} \| [SL]J_j \rangle|^2 \quad (5)$$

where μ_B is the Bohr magneton. $\mathbf{L}$ and $\mathbf{S}$ are the angular momentum and spin operators, respectively. The matrix elements of $\mathbf{L} + 2\mathbf{S}$ can be found elsewhere.[29]

The rate of multiphonon relaxation, $W_{i,i-1}^{NR}$, can be determined using Van Dijk's modified Energy Gap Law[31,32,37]

$$W_{i,i-1}^{NR} = W_{MPR}^0 \exp[-\alpha(\Delta E - 2h\omega_{max})] \quad (6)$$

ΔE (cm^{-1}) is the energy gap to the lower manifold; $h\omega_{max}$ is the highest phonon energy of the host matrix; and W_{MPR}^0 (s^{-1}) and α (cm) are constants specific to each host matrix.

For an isolated donor–acceptor pair, the orientation-averaged rate of dipole–dipole energy transfer, $W_{ij,kl}^{ET}$, with donor transition $i \rightarrow j$ and acceptor transition $k \rightarrow l$, can be described as a function of the interion distance R and the line strengths of the acceptor and donor transitions as determined by J–O theory[33,38]

$$W_{ij,kl}^{ET} = \frac{C_{DA,ijkl}}{R^6} \quad (7)$$

$$C_{DA,ijkl} = \frac{8\pi^2 e^4 s_0}{3h^2 c g_i g_k} \left(\frac{n^2+2}{3n} \right)^4 S_{ij}^{ED} S_{kl}^{ED} \quad (8)$$

C_{DA} is the energy transfer microparameter; g_i is the $2J + 1$ number of states in manifold i; and s_0 (cm) is the overlap integral between the normalized donor emission spectrum and acceptor absorption spectrum.

Since most energy transfer processes are not resonant and require the emission or absorption of phonons to conserve energy, Miyakawa and Dexter[32] modified the expression for resonant energy transfer rates with an exponential dependence related to the Energy Gap Law. We can then write the phonon-assisted energy transfer microparameter as

$$C_{DA}^{PAET} = C_{DA}^0 \exp[-\beta_{MPR} \Delta E] \quad (9)$$

where β_{MPR} is a material-dependent constant related to the MPR constant α,[32] and ΔE is the net energy difference between the donor and acceptor transitions. C_{DA}^0 is the energy transfer microparameter assuming a resonant ET process.

For the relatively high dopant concentrations considered in this work, resonant donor–donor energy migration is faster than donor–acceptor energy transfer, resulting in a uniform distribution of excited donors. The rate constant for migration-

dx.doi.org/10.1021/jp302401j | J. Phys. Chem. B XXXX, XXX, XXX–XXX

assisted energy transfer in the fast migration limit can be calculated to be[39]

$$P_{ij,kl}^{\mathrm{MAET}} = \frac{4\pi}{3} C_{\mathrm{DA},ijkl}^{\mathrm{PAET}} \left({R_{\mathrm{min}}}^{-3} - \frac{4\pi}{3} N_k \right) \tag{10}$$

where R_{min} is the minimum donor−acceptor distance allowed by the crystal structure of the host matrix.

EXPERIMENTAL AND THEORETICAL METHODS

Simulation. Using the aforementioned theoretical framework, we developed a computational model that generates rate constants for all possible transitions, numerically solves the simultaneous differential equations for the relevant manifolds (eq 1), and calculates the resulting spectra. We calculated most rate constants using published J−O parameters[40] for β-$NaYF_4$ or from experimental measurements. Since β-$NaYF_4$ is poorly characterized in bulk form, we supplemented parameters with those measured for other sodium yttrium fluoride crystals and other metal fluorides (e.g., LaF_3,[31] $LiYF_4$[41]), which have phonon energies similar to β-$NaYF_4$.[42] We adjusted only the MPR parameters, which would logically vary from bulk values due increased surface effects[43] and due to confinement effects on phonon propagation.[7] Additional modeling details are given in the Supporting Information.

Emission intensities were simulated by calculating the photon emission rates, $N_i(A_{ij}^{\mathrm{ED}} + A_{ij}^{\mathrm{MD}})$, for each manifold i. In all cases, the simulations considered 10 W/cm^2 illumination at 980 nm. Theoretical quantum yields were calculated by dividing the overall photon emission rate at a given energy by the photon absorption rate, which for Er^{3+}-containing systems was indistinguishable from the overall rate (ED + MD) of the Er^{3+}:$^4I_{15/2} \rightarrow {}^4I_{11/2}$ transition.

Spectral Purity. We quantified the spectral purity, SP, of the nanocrystals' upconversion luminescence (UCL) using the equation

$$\mathrm{SP} = \frac{a_g - a_r}{a_g + a_r} \tag{11}$$

For simulated spectra, $a_x = N_i(A_{ij}^{\mathrm{ED}} + A_{ij}^{\mathrm{MD}})$ where $j = {}^4I_{15/2}$ and $i = {}^4S_{3/2}$ ($^4F_{9/2}$) for $x = g(r)$. For experimental measurements, a_g and a_r are the integrated areas from 500 to 600 nm and 600 to 700 nm, respectively. SP values of +1, −1, and 0 correspond, respectively, to exclusively green emission, exclusively red emission, and equal intensities of green and red emission.

Pathway Analysis. To determine the most important transitions for a given energy transfer pathway, we considered only transitions with the highest branching fractions (β_{ij}) or contribution fractions (κ_{ij}), where

$$\beta_{ij,t} = \frac{\left(\frac{dN_i}{dt}\right)_{i\rightarrow j}^{t}}{\sum\limits_{\substack{t=\mathrm{ED,MD,}\\ \mathrm{ET,MPR}}} \sum\limits_{m} \left(\frac{dN_i}{dt}\right)_{i\rightarrow m}^{t}} \tag{12}$$

$$\kappa_{ij,t} = \frac{\left(\frac{dN_j}{dt}\right)_{i\rightarrow j}^{t}}{\sum_t \sum_m \left(\frac{dN_j}{dt}\right)_{m\rightarrow j}^{t}} \tag{13}$$

For a given transition type t (ED/MD radiative, ET, MPR) from i to j, κ_{ij} (β_{ij}) represents that transition's fractional contribution to the overall population (depletion) of j (i) by all types of transitions to (from) level j (i). The rates dN_i/dt are determined by the populations of the originating states and the corresponding microscopic rate constants, as shown by the individual components of eq 1.

To select the most significant incoming transitions for each manifold i, we retained the transitions with the highest κ_{ij} that cumulatively contributed to over 90% of the respective population of j (i.e., $\Sigma\kappa_{ij} > 0.90$). The most significant depopulating transitions can be filtered similarly using β_{ij} values.

To determine the critical energy transfer pathways for conferring spectrally pure emission, we selected a transition of interest, $m_o \rightarrow m_f$, and examined the most significant transitions that populated the originating state, m_o. We recursively investigated each of these incoming transitions in the same manner, until the transitions looped back onto themselves or terminated at a ground state. Similar path tracing can be performed in the forward direction starting from the ground state absorption of incident photons and investigating the transitions with the highest branching fractions out of the final state(s) of each transition.

Synthesis of Lanthanide-Doped $NaYF_4$ Nanocrystals. Hexagonal β-$NaYF_4$ nanocrystals doped with Er^{3+}, Tm^{3+}, or other lanthanide ions were synthesized using a combinatorial, high-throughput method in which an automated nanocrystal synthesis robot[44] dispensed oleylamine-based stock solutions of the trifluoroacetate[45] salts of sodium, yttrium, and lanthanide dopants into 1 mL glass vials loaded in a 96-well aluminum reactor block. The reactor block was heated to 300 °C for 1 h to produce $NaYF_4$ nanocrystals, which were then isolated from the reaction solution using repeated dissolution with chloroform, precipitation with ethanol and methanol, and centrifuging to separate the nanoparticle solids. Larger batches of nanocrystals were synthesized by heating mixtures of lanthanide chlorides, ammonium fluoride, sodium oleate, oleic acid, and octadecene.[10] Typical rare earth ion concentrations in reaction solutions were 25 mM, and the mole percent of the dopants in the nanocrystals (e.g., 2% mol Er^{3+} = $NaY_{0.98}Er_{0.02}F_4$) mirrored the stoichiometry of the precursors, an observation verified to be within 5% accuracy for several samples using elemental analysis (ICP-OES).

Characterization. Upconverted luminescence spectra were measured on UCNP samples dried in the wells of a white round-bottom polypropylene microplate (Corning) using the Micromax plate reader attachment of a Fluorolog-3 spectrometer (Horiba Jobin Yvon). Samples were excited at 980 nm (10 W/cm^2) using a fiber optic diode laser (Sheaumann) filtered with an 850 nm long-pass filter (Thorlabs), replicating the conditions considered in the simulations. Emission was filtered through a 785 nm short pass filter (Semrock). The detection bandwidth was 5 nm for high-throughput screening. After background subtraction, intensity values were corrected for instrumental response using the spectrum of a calibrated light source (ASD) then further corrected for the transmission spectrum of the emission filter. Absolute quantum yields were measured in an integrating sphere[10] using procedures detailed in the Supporting Information. Upconversion luminescence lifetimes were obtained with a 980 nm diode laser (Thorlabs) modulated at 250 Hz and measured with an avalanche photodiode (Micro Photon Devices) coupled to a time-

dx.doi.org/10.1021/jp302401j | J. Phys. Chem. B XXXX, XXX, XXX−XXX

correlated single photon counter (Picoquant). Transmission electron microscopy was performed on a JEOL 2100 microscope at 200 kV.

RESULTS AND DISCUSSION

Theoretical Validation. Having established the theoretical model and computational framework detailed above, we sought to validate their output using UCL spectra from $NaYF_4$ nanocrystals (Figure 1a) synthesized with a range of Er^{3+} and

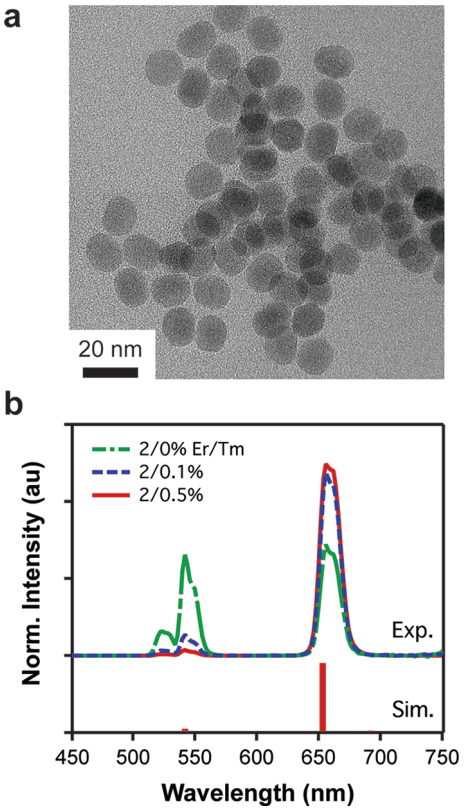

Figure 1. (a) Transmission electron micrograph of $NaYF_4$:Er^{3+}/Tm^{3+} nanocrystals. (b) Experimental and simulated upconversion luminescence spectra of $NaYF_4$ nanocrystals doped with 2% Er^{3+} and three different concentrations of Tm^{3+} with 980 nm (10 W/cm^2) excitation.

Tm^{3+} concentrations. Compared with $NaYF_4$ nanocrystals doped with only Er^{3+}, which displayed red and green upconversion luminescence peaks typical of those reported previously,[42] $NaYF_4$ nanocrystals doped with both Er^{3+} and Tm^{3+} exhibited much stronger red emission (660 nm, Er^{3+}:$^4F_{9/2}$ → $^4I_{15/2}$) and dramatically weaker green emission (525/540 nm, Er^{3+}:$^2H_{11/2}$/$^4S_{3/2}$ → $^4I_{15/2}$) in their normalized UCL spectra (Figure 1b). Er^{3+}/Tm^{3+}-doped UCNPs exhibited increasingly pure red emission at higher Tm^{3+} concentration, with the spectral purity saturating (|SP| > 95%) at 0.5% Tm^{3+} (Figure 2). This strong concentration dependence is reasonable given the role of energy transfer in previously proposed mechanisms, yet we also observed that spectral purity was insensitive to Er^{3+} concentration (Figure 2b), even over a broad range of Tm^{3+} concentrations.

Spectra calculated from numerical solutions (Figure 1b) exhibited spectral purity values that fit experimental data within measurement error for 1% and 2% Er^{3+} and 0.1−3.0% Tm^{3+} (Figure 2b). Theoretical values varied slightly from experiment for UCNPs doped with a combination of 10% Er^{3+} and 0.1−

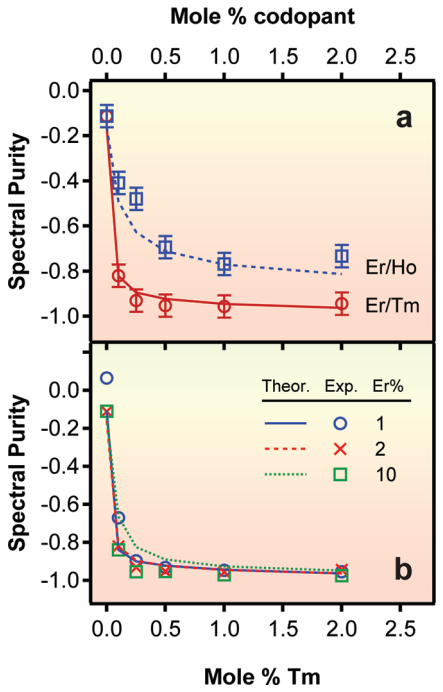

Figure 2. (a) Experimentally measured (symbols) and theoretically calculated (lines) spectral purities of $NaYF_4$:Er^{3+}/Ho^{3+} and $NaYF_4$:Er^{3+}/Tm^{3+} at 2% Er^{3+} and six codopant concentrations. (b) Theoretical and observed spectral purities of $NaYF_4$:Er^{3+}/Tm^{3+} at three Er^{3+} concentrations and six Tm^{3+} concentrations. Spectra were measured and simulated with 980 nm excitation at 10 W/cm^2. Error bars in (a) reflect experimental uncertainty of SP ± 0.05.

0.5% Tm^{3+}. Considering that our model does not account for variations in microscopic rate constants as dopants reach extremely high concentrations (10%), we consider the theoretical predictions to be generally very accurate. As shown in Figure 2a, our model also accurately simulated the spectral purities of UCNPs doped with Er^{3+}/Ho^{3+} (Figure 2a). Theoretical luminescence lifetimes and quantum yields for 10/0.5% Er^{3+}/Tm^{3+} fell within a factor of 2 of values measured using 10 W/cm^2 excitation at 980 nm (Supporting Information, Table S1). Thus, our model is well-validated across a wide range of compositions, concentrations, and experimental parameters.

Population Enhancement in Er^{3+}/Tm^{3+}. The intensity of upconverted luminescence at a given wavelength is proportional to the product of the population of a manifold and the microscopic radiative rate constant. If we assume, as our model does, that the Judd−Ofelt parameters and therefore the radiative rate constants are independent of dopant concentration, the introduction of Tm^{3+} to Er^{3+}-doped UCNPs must promote spectrally pure red emission by populating red emitting manifolds and/or depopulating green-emitting manifolds. Indeed, the simulated addition of 2% Tm^{3+} to 2% Er^{3+} induced a 5-fold increase in the steady state Er^{3+}:$^4F_{9/2}$ population and a 7-fold decrease in the steady state Er^{3+}:$^4S_{3/2}$ population (Table 1)—moves that were mirrored by identical changes in the emission rates of the corresponding transitions (Table 2 and Supporting Information, Table S2). In addition, the populations of Er^{3+}:$^4I_{13/2}$ and $^4I_{11/2}$, which play essential roles in the Er^{3+} upconversion pathway, decreased by 97% and 64%, respectively.

dx.doi.org/10.1021/jp302401j | J. Phys. Chem. B XXXX, XXX, XXX−XXX

Table 1. Steady State Populations in $NaYF_4$:Er^{3+} (2%) and Er^{3+}/Tm^{3+} (2/2%)[a]

level i	$^{2S+1}L_J$	energy (cm^{-1})	N_i (nm^{-3}), 2% Er^{3+}	N_i (nm^{-3}), 2/2% Er^{3+}/Tm^{3+}	$N_{i,Er/Tm}/N_{i,Er}$
Er^{3+}					
0	$^4I_{15/2}$	0	2.645×10^{-1}	2.752×10^{-1}	1.04
1	$^4I_{13/2}$	6632	9.747×10^{-3}	2.529×10^{-4}	0.03
2	$^4I_{11/2}$	10230	2.018×10^{-3}	7.267×10^{-4}	0.36
3	$^4I_{9/2}$	12553	1.064×10^{-5}	5.990×10^{-6}	0.56
4	$^4F_{9/2}$	15306	5.005×10^{-6}	2.795×10^{-5}	5.58
5	$^4S_{3/2}$	18448	3.995×10^{-6}	5.866×10^{-7}	0.15
6	$^2H_{11/2}$	19246	2.010×10^{-8}	5.654×10^{-10}	0.03
7	$^4F_{7/2}$	20497	5.156×10^{-9}	2.172×10^{-9}	0.42
8	$^4F_{5/2}$	22282	4.420×10^{-10}	7.535×10^{-10}	1.70
9	$^4F_{3/2}$	22677	2.052×10^{-12}	4.987×10^{-12}	2.43
Tm^{3+}					
10	$^3H_6$	153		2.576×10^{-1}	
11	$^3F_4$	5828		1.867×10^{-2}	
12	$^3H_5$	8396		1.419×10^{-5}	
13	$^3H_4$	12735		2.242×10^{-5}	
14	$^3F_3$	14598		4.479×10^{-7}	
15	$^3F_2$	15180		2.781×10^{-9}	
16	$^1G_4$	21352		1.132×10^{-8}	
17	$^1D_2$	28028		1.656×10^{-10}	

[a]Calculated at 980 nm (10 W/cm^2) excitation

Table 2. Major Branching Transitions for $NaYF_4$:Er^{3+}/Tm^{3+}(2/2%) Calculated at the Steady State

level i	transition type	transition $i \rightarrow j$[a]	rate (nm^{-3}/s)	β_{ij}
Er^{3+}:$^4I_{13/2}$	ET donor	$^4I_{13/2} \rightarrow {}^4I_{15/2}$ (Tm^{3+}:$^3H_6 \rightarrow {}^3F_4$)	5.217	0.963
Er^{3+}:$^4I_{11/2}$	ET acceptor	$^4I_{11/2} \rightarrow {}^4F_{9/2}$ (Tm^{3+}:$^3F_4 \rightarrow {}^3H_6$)	3.449	0.416
	MPR	$^4I_{11/2} \rightarrow {}^4I_{13/2}$	3.284	0.396
	ET donor	$^4I_{11/2} \rightarrow {}^4I_{13/2}$ (Tm^{3+}:$^3F_4 \rightarrow {}^3H_5$)	0.863	0.104
	ED abs.	$^4I_{11/2} \rightarrow {}^4F_{7/2}$	0.019	0.002
Er^{3+}:$^4F_{9/2}$	MPR	$^4F_{9/2} \rightarrow {}^4I_{9/2}$	2.433	0.702
	ET donor	$^4F_{9/2} \rightarrow {}^4I_{15/2}$ (Tm^{3+}:$^3H_6 \rightarrow {}^3F_3$)	0.426	0.123
	ET donor	$^4F_{9/2} \rightarrow {}^4I_{15/2}$ (Tm^{3+}:$^3H_6 \rightarrow {}^3F_2$)	0.257	0.074
	ED rad.	$^4F_{9/2} \rightarrow {}^4I_{15/2}$	0.029	0.008
Er^{3+}:$^4S_{3/2}$	ET donor	$^4S_{3/2} \rightarrow {}^4I_{9/2}$ (Tm^{3+}:$^3H_6 \rightarrow {}^3F_4$)	0.031	0.649
	MPR	$^4S_{3/2} \rightarrow {}^4F_{9/2}$	0.013	0.273
	ED rad.	$^4S_{3/2} \rightarrow {}^4I_{15/2}$	0.001	0.011
Tm^{3+}:$^3F_4$	ET donor	$^3F_4 \rightarrow {}^3H_6$ (Er^{3+}:$^4I_{11/2} \rightarrow {}^4F_{9/2}$)	3.449	0.384
	ED rad.	$^3F_4 \rightarrow {}^3H_6$	2.353	0.262
	ET acceptor	$^3F_4 \rightarrow {}^3H_5$ (Tm^{3+}:$^3F_4 \rightarrow {}^3H_6$)	0.883	0.098
	ET donor	$^3F_4 \rightarrow {}^3H_6$ (Tm^{3+}:$^3F_4 \rightarrow {}^3H_5$)	0.883	0.098
	ET acceptor	$^3F_4 \rightarrow {}^3H_5$ (Er^{3+}:$^4I_{11/2} \rightarrow {}^4I_{13/2}$)	0.863	0.096
Tm^{3+}:$^3H_5$	MPR	$^3H_5 \rightarrow {}^3F_4$	2.364	0.966

[a]Transitions in parentheses denote complementary ET transition.

Strong Energy Transfer from Tm^{3+}:$^3F_4$ Induces Spectrally Pure Red Emission. While steady state populations provide the macroscopic justification for selective UC emission in Er^{3+}/Tm^{3+}-doped $NaYF_4$, we sought to uncover the microscopic processes that contribute to the population of the red-emitting manifold and the depopulation of other states. Working backward from the red-emitting Er^{3+}:$^4F_{9/2}$ manifold and the green-emitting $Er^{3+2}H_{11/2}$ and $^4S_{3/2}$ manifolds, we used the aforementioned pathway analysis algorithm to isolate, out of the thousands of transitions calculated by our model, the processes most responsible for populating and depopulating those states in UCNPs doped with Er^{3+} and Er^{3+}/Tm^{3+} (Tables 2 and 3).

The mechanism for UCNPs doped only with Er^{3+} (Figure 3a), which we consider for reference, shows the population of the green-emitting Er^{3+}:$^2H_{11/2}$ and $^4S_{3/2}$ levels via ground state absorption (GSA) to the $^4I_{11/2}$ manifold, followed by excited state absorption (ESA) or energy transfer upconversion (ETU Step 0, or ETU0, Figure 3a) and subsequent nonradiative relaxation (MPR). While the red-emitting $^4F_{9/2}$ state can be populated by further MPR from the $^4S_{3/2}$ manifold, pathway analysis shows that the dominant pathway for $^4F_{9/2}$ population is the ETU Step 1 (ETU1, Figure 3a, κ_{ij} = 0.75), in which an ion in the $^4I_{13/2}$ manifold donates all of its energy to an acceptor ion in the $^4I_{11/2}$ manifold.

dx.doi.org/10.1021/jp302401j | J. Phys. Chem. B XXXX, XXX, XXX–XXX

Table 3. Major Contributing Transitions for $NaYF_4:Er^{3+}/Tm^{3+}$(2/2%) Calculated at the Steady State

level j	transition type	transition $i \rightarrow j$	rate (nm^{-3}/s)	κ_{ij}
$Er^{3+}:{}^4I_{13/2}$	MPR	${}^4I_{11/2} \rightarrow {}^4I_{13/2}$	3.284	0.606
	ET donor	${}^4I_{11/2} \rightarrow {}^4I_{13/2}$ ($Tm^{3+}:{}^3F_4 \rightarrow {}^3H_5$)	0.863	0.159
	ET acceptor	${}^4I_{15/2} \rightarrow {}^4I_{13/2}$ ($Tm^{3+}:{}^3H_4 \rightarrow {}^3F_4$)	0.658	0.121
$Er^{3+}:{}^4I_{11/2}$	ED abs.	${}^4I_{15/2} \rightarrow {}^4I_{11/2}$	5.865	0.708
	MPR	${}^4I_{9/2} \rightarrow {}^4I_{11/2}$	2.356	0.284
$Er^{3+}:{}^4F_{9/2}$	ET acceptor	${}^4I_{11/2} \rightarrow {}^4F_{9/2}$ ($Tm^{3+}:{}^3F_4 \rightarrow {}^3H_6$)	3.449	0.995
$Tm^{3+}:{}^3F_4$	ET acceptor	${}^3H_6 \rightarrow {}^3F_4$ ($Er^{3+}:{}^4I_{13/2} \rightarrow {}^4I_{15/2}$)	5.217	0.581
	MPR	${}^3H_5 \rightarrow {}^3F_4$	2.364	0.263
	ET donor	${}^3H_4 \rightarrow {}^3F_4$ ($Er^{3+}:{}^4I_{15/2} \rightarrow {}^4I_{13/2}$)	0.658	0.073
$Tm^{3+}:{}^3H_5$	ET acceptor	${}^3F_4 \rightarrow {}^3H_5$ ($Tm^{3+}:{}^3F_4 \rightarrow {}^3H_6$)	0.883	0.361
	ET acceptor	${}^3F_4 \rightarrow {}^3H_5$ ($Er^{3+}:{}^4I_{11/2} \rightarrow {}^4I_{13/2}$)	0.863	0.353
	ET acceptor	${}^3H_6 \rightarrow {}^3H_5$ ($Er^{3+}:{}^4I_{11/2} \rightarrow {}^4I_{15/2}$)	0.361	0.147

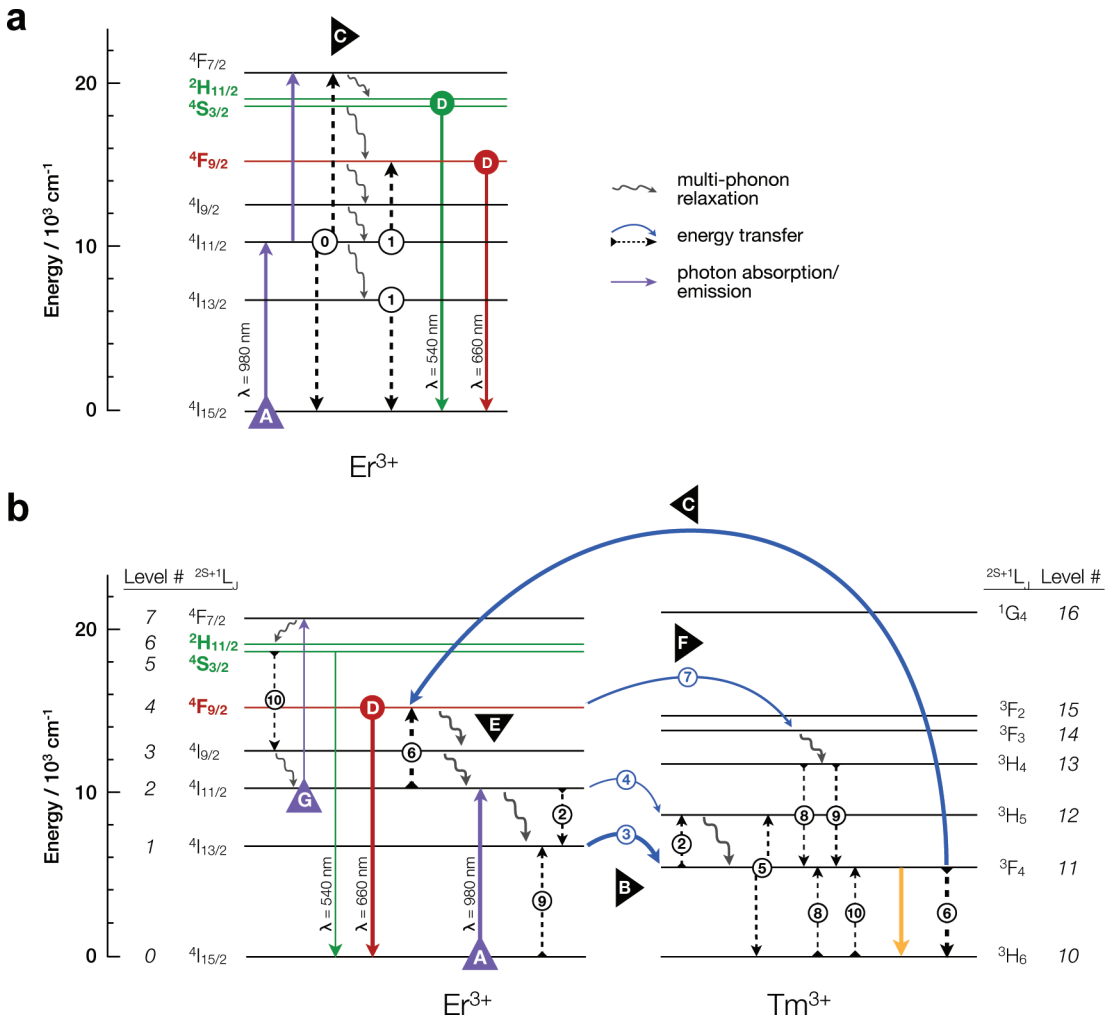

Figure 3. Energy level diagrams and major steady state transition pathways for $NaYF_4$ nanocrystals doped with 2% Er^{3+} (a) and 2% Er^{3+}/2% Tm^{3+} (b). The major pathways (filled symbols) are photon absorption (A), energy concentration and storage (B), population of the emitting manifold via energy transfer upconversion (C), luminescence (D), and energy recycling via multiphonon relaxation (E) or via energy transfer/cross relaxation (F). The minor pathway for the population of green-emitting manifolds (G) is shown in (b).

In materials doped with Er^{3+} and Tm^{3+}, however, green emission is quenched by 85% because the rates of the ESA and ETU0 pathways that ultimately populate $Er^{3+}:{}^2H_{11/2}/{}^4S_{3/2}$ decrease linearly and quadratically, respectively, with the 3-fold reduction in the population of their originating $Er^{3+}:{}^4I_{11/2}$ manifold. In addition, the green emission is reduced by an ET process (ET10, Figure 3b) that outcompetes radiative relaxation for the depopulation of $Er^{3+}:{}^2H_{11/2}$ and ${}^4S_{3/2}$ (β_{ij} = 0.65, Table 2). Thus, the 7-fold reduction in green emission in Er^{3+}/Tm^{3+} can be rationalized by the effective quenching of pathways in Er^{3+} that populate green-emitting states and by the introduction of ET pathways that depopulate those states.

Conversely, red emission in Er^{3+}/Tm^{3+}-doped $NaYF_4$ is enhanced dramatically by introduction of ET pathways that

dx.doi.org/10.1021/jp302401j | J. Phys. Chem. B XXXX, XXX, XXX–XXX

Scheme 1. Emission, Population, and Energy Recycling Pathways in $NaYF_4:Er^{3+}/Tm^{3+}$

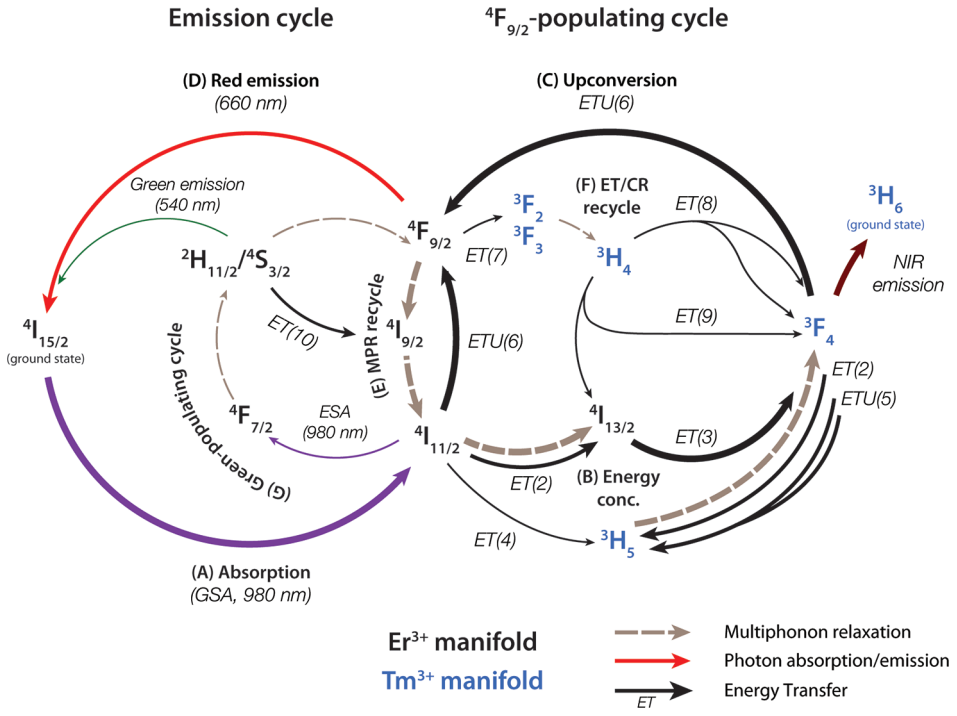

populate the red-emitting manifold. Unlike $NaYF_4:Er^{3+}$, the Er^{3+}:$^4F_{9/2}$ manifold in $NaYF_4:Er^{3+}/Tm^{3+}$ is almost exclusively populated by ETU6 (κ_{ij} = 0.995, Table 3), as depicted in the mechanism in Figure 3b. Here, a donor Tm^{3+} ion excited in the $^3F_4$ manifold completely transfers its energy to an acceptor Er^{3+} ion in its $^4I_{11/2}$ manifold, resulting in population of the Er^{3+}:$^4F_{9/2}$ manifold. The critical role of ETU6 to enhanced red emission has been proposed by several authors,[24,25,27] but its significance relative to alternate pathways has not been discussed quantitatively. Underscoring the importance of this pathway, the 3.4 nm^{-3}/s rate of ETU6 is nearly 60% of the resonant ground state absorption rate of 5.9 nm^{-3}/s (Table 3).

The substantial rate of ETU6 is partially a consequence of its large energy transfer microparameter, C_{DA}, which is proportional to the line strengths of the Er^{3+}:$^4I_{11/2} \rightarrow {}^4F_{9/2}$ and Tm^{3+}:$^3F_4 \rightarrow {}^3H_6$ transitions (eq 8). These donor and acceptor S^{ED} values are greater than 90% of the S^{ED} for all transitions in their respective ions. A second contributor to the large rate of ETU6 is the high steady state population the donor Tm^{3+}:$^3F_4$ manifold. At 7% of the overall Tm^{3+} concentration (Table 1), the $^3F_4$ population is over 25 times the population of any other excited manifold in the Er^{3+}/Tm^{3+} system, explaining the selectivity and efficiency of the upconversion processes in Er^{3+}/Tm^{3+}-codoped materials.

We can calibrate the significance of each component of the ETU6 process (Figure 3b) to the red spectral purity of Er^{3+}/Tm^{3+} by comparing ETU6 to the analogous, Er^{3+}:$^4F_{9/2}$-populating ETU1 process in $NaYF_4:Er^{3+}$ (Figure 3a), which has near-zero SP. Although the acceptors in both ETU processes undergo the same Er^{3+}:$^4I_{11/2} \rightarrow {}^4F_{9/2}$ transition, the rate of ETU6 is 10 times greater than that of ETU1, a discrepancy that must be attributed to the different donor transitions. Initially considering the population dependence of the ETU rate, we note that the donor Tm^{3+}:$^3F_4$ population in ETU6 is double that of the donor Er^{3+}:$^4I_{13/2}$ manifold in ETU1, but the population of the common acceptor, Er^{3+}:$^4I_{11/2}$, is reduced by 64% by the addition of 2% Tm^{3+} (Table 1). Therefore, the combined $N_{donor}{\cdot}N_{acceptor}$ contribution to the rate of ETU6 (eq 1) is actually *lower* than that of ETU1 and thus cannot explain the enhanced rate of ETU6.

When we examine the ET rate constants, we note that the $S_{donor}^{ED}{\cdot}S_{acceptor}^{ED}$ contributions to the C_{DA} of ETU6 and ETU1 are also comparable (eq 8). However, C_{DA} is inversely proportional to the $2J + 1$ multiplicity of the donor manifold (eq 8), with $2J + 1 = 9$ for Tm^{3+}:$^3F_4$ and 27 for Er^{3+}:$^4I_{13/2}$. This 3-fold multiplicity ratio explains why the C_{DA} of ETU6, without phonon assistance, is three times greater than that of ETU1. Our physical interpretation of this phenomenon is that, when a donor manifold has fewer states, the concentration of the energy in those states leads to greater coupling for the individual state-to-state transitions and therefore a higher aggregate ET rate.

Finally, we consider that the phonon-assisted ET rate constant C_{DA}^{PAET} varies exponentially with the ET energy gap. The 1560 cm^{-1} downhill energy gap of ETU1 is substantially wider than the slightly downhill 600 cm^{-1} energy gap of ETU6, resulting in ETU1 having a 6.5-fold greater penalty for phonon assistance, $\exp(-\beta_{MPR}\Delta E_{gap})$. Having zero energy gap, as is the case for the analogous ETU process in Er^{3+}/Ho^{3+}, would not necessarily enhance spectral purity because resonant back transfer can reduce the net energy transfer rate. We therefore conclude that a slightly downhill energy gap is optimal for discouraging back transfer without requiring the excessive emission of phonons. Thus, optimal energy level alignment and stronger coupling of the transitions on the donor and acceptor are the key factors that explain the large rate of ETU6 in $NaYF_4:Er^{3+}/Tm^{3+}$ relative to the analogous ETU steps in $NaYF_4:Er^{3+}$ and other Er^{3+}-codoped materials.

Energy Transfer Pathways in Er^{3+}/Tm^{3+}. We used pathway analysis similar to that used for the population of the red-emitting Er^{3+}:$^4F_{9/2}$ state to map all of the major

dx.doi.org/10.1021/jp302401j | J. Phys. Chem. B XXXX, XXX, XXX–XXX

pathways and connect them in a single holistic mechanism that highlights the interrelated transitions responsible for populating each manifold. The mechanism depicted on the energy level diagram in Figure 3b clearly details the relationship between the transition pathways and the alignment of energy levels, which we already noted was a critical factor for spectrally pure red emission. However, we find that displaying the mechanisms as energy-agnostic flowcharts (Scheme 1) better highlights the convergence and divergence of energy through specific Er^{3+} and Tm^{3+} excited states so that we can rationalize the relative significance of pathways (indicated by the weight of the arrows) and understand their cyclical and interconnected relationships. Thus, we will use both mechanistic representations to explain the major transition pathways of the Er^{3+}/Tm^{3+} codopant system.

Starting with the donor of the red-emission-promoting ETU6 process (Pathway C, Figure 3b), we find that Tm^{3+}:$^3F_4$ is predominantly populated via Pathway B (Figure 3b), in which ET3—with the help of ET2, ET4, and associated MPR steps—transfers energy from Er^{3+}:$^4I_{11/2}$ to Tm^{3+}:$^3F_4$. As evinced by the low populations of the Er^{3+}:$^4I_{11/2}$ and $^4I_{13/2}$ states and the high population of Tm^{3+}:$^3F_4$, this pathway is extremely efficient at transferring energy from Er^{3+} into the Tm^{3+}:$^3F_4$ manifold, which serves to concentrate, store, and donate energy via the important ETU6 transition.

Er^{3+}:$^4I_{11/2}$, itself an originating state for ETU6 and its Pathway B tributary, is populated predominantly by Er^{3+} ground state absorption of 980 nm photons (Pathway A, κ_{ij} = 0.71) . This $^4I_{11/2}$ manifold also receives energy via sequential MPR from Er^{3+}:$^4F_{9/2}$ (Pathway E, κ_{ij} = 0.28), effectively "recycling" the energy not used for radiative emission. Energy can also be recycled from Er^{3+}:$^4F_{9/2}$ to Tm^{3+}:$^3F_4$ via ETU steps 7−9 (Pathway F, Figure 3b). We will discuss the implications of this energy recycling in a later section.

Having traced the flow of energy in the coupled Er^{3+}/Tm^{3+} system, we can view the ensemble mechanism as an interconnected network of six major pathways (Figure 3b and Scheme 1): the ground state absorption by Er^{3+} (Pathway A), the transfer of energy from Er^{3+}:$^4I_{11/2}$ and concentration into Tm^{3+}:$^3F_4$ (B), ETU population of the red-emitting $^4F_{9/2}$ manifold (C), the radiative emission of 660 nm photons (D), and the recycling of energy via MPR (E) and via ET/cross-relaxation (F). These fundamental pathways intersect at three major nodes—the emitting state (Er^{3+}:$^4F_{9/2}$), a routing state (Er^{3+}:$^4I_{11/2}$) that receives and disperses absorbed energy, and a storage state (Tm^{3+}:$^3F_4$) that concentrates energy for selective population of the emitting state. These nodes are clearly demarcated by their multitude of incoming and outgoing transitions. These nodes link the pathways and form the nexuses of two major cycles (Scheme 1) that represent (1) the continual population of the red-emitting Er^{3+}:$^4F_{9/2}$ state (Pathway B → C → E → B) and (2) the excitation and spectrally pure emission from that state (A → C → D → A). Minor cycles highlight the multiplying effect of the ET/cross-relaxation pathway (F) and the insignificance of the "green", or Er^{3+}:$^2H_{11/2}$/$^4S_{3/2}$-populating, cycle (G). As a whole, this set of pathways demonstrates that, while the rapid rate of ETU6 is the most direct cause, the coordination and balance of all of the pathways (A−F) are essential for the population and depopulation of the intermediate states that ultimately give rise to the spectrally pure red emission in Er^{3+}/Tm^{3+}-doped materials.

Energy Conservation, Recycling, And the Origins of Enhanced UCL Efficiency. Having elucidated the origins of the spectrally pure red emission of $NaYF_4$:Er^{3+}/Tm^{3+} using the pathways in Scheme 1, we sought to explain our 2-fold increase in quantum yield (Supporting Information, Table S1) and the similar increases reported by others.[24−26] From the pathway cycles in Scheme 1, it is apparent that the same mechanisms that promote spectral purity in Er^{3+}/Tm^{3+} also contribute to the enhanced intensity in the red UCL. Rather than discarding the energy from unwanted transitions, the presence of Tm^{3+} diverts energy away from green emission pathways in Er^{3+} and adds this energy to pathways that populate red-emitting states, thereby increasing the efficiency and intensity of red emission. The energy concentration pathway (B) so efficiently depopulates the Er^{3+}:$^4I_{11/2}$ node that only 0.2% of its population participates in ESA absorption (Table 2) and that no energy is used for ETU from this manifold (ETU0, Figure 3a). Once delivered to Pathway C, this energy can more efficiently populate the red-emitting manifold because ETU6 is 15 times more efficient than the analogous ETU1 pathway in $NaYF_4$:Er^{3+} (Figure 3).

At the Tm^{3+}:$^3F_4$ node, energy is conserved within the Er^{3+}:$^4F_{9/2}$-populating pathway because the large rate of ETU6 reduces the branching ratio of the strong Tm^{3+}:$^3F_4$ → $^3H_6$ radiative relaxation to β_{ij} = 0.26 (Table 2). Moreover, the 5800 cm^{-1} energy gap below Tm^{3+}:$^3F_4$ eliminates any significant energy loss via MPR. Once again, we observe how the strong donor−acceptor coupling of ETU6 and the electronic structure of Tm^{3+} contribute to the distinctive optical properties of Er^{3+}/Tm^{3+}.

Energy losses through MPR and undesirable radiative emission are minimized in $NaYF_4$:Er^{3+}/Tm^{3+} because the transition pathways E and F recycle energy that Er^{3+}:$^4F_{9/2}$ does not emit radiatively back into the $^4F_{9/2}$-populating pathway (Scheme 1). In the major recycling pathway (Pathway E, β_{ij} = 78%), MPR from Er^{3+}:$^4F_{9/2}$ contributes 28% of the population of Er^{3+}:$^4I_{11/2}$ (Table 3). Since only 5100 cm^{-1} of the 15 300 cm^{-1} energy of $^4F_{9/2}$ is released through phonon emission, this MPR recycling pathway is ∼67% efficient from an energy perspective. In the minor ET-recycling pathway (E), Tm^{3+} excited ions in their $^3H_4$ manifolds can undergo cross-relaxation (CR) via ET8 and ET9 that, with the help of ET3, produces two Tm^{3+} ions excited in the $^3F_4$ manifold for every donor ion. This process avoids energy relaxation via MPR, leading to 76% energy efficiency and contributing to 18% of the large Tm^{3+}:$^3F_4$ population. While these MPR and ET recycling pathways actually compete with radiative emission of red photons and reduce the quantum yield, this decrease in QY is minimized by the fact that these recycling pathways return energy back to the major Er^{3+}:$^4F_{9/2}$ -populating pathway with high efficiency.

CONCLUSIONS

We have elucidated, theoretically and quantitatively, the mechanistic origins of the spectrally pure red upconverted luminescence of Er^{3+}/Tm^{3+}-codoped $NaYF_4$ nanocrystals. Using a kinetic model validated by high-throughput experimental data and using an unbiased path-tracing algorithm to identify the most significant populating and depopulating transitions, we have revealed a mechanism in which energy is diverted away from the Er^{3+}:$^2H_{11/2}$/$^4S_{3/2}$ green-emitting manifolds and is concentrated and effectively stored in the low-lying Tm^{3+}:$^3F_4$ first-excited state. This heavily populated Tm^{3+}:$^3F_4$ manifold then donates all of its energy to an Er^{3+} ion

dx.doi.org/10.1021/jp302401j | J. Phys. Chem. B XXXX, XXX, XXX−XXX

in the $^4I_{11/2}$ manifold to populate the red-photon-emitting Er^{3+}:$^4F_{9/2}$ manifold. The strength of this ETU6 transition, representing 60% of the Er^{3+} ground state absorption rate, is a function of (1) the enhanced coupling of the Tm^{3+}:$^3F_4$ manifold and its ground state, (2) the slightly downhill energetics of ETU6, and (3) the large population of Tm^{3+}:$^3F_4$. These factors, along with the ability to recycle energy not utilized for red emission, also contribute to the enhanced quantum yield of $NaYF_4$:Er^{3+}/Tm^{3+} relative to $NaYF_4$:Er^{3+}.

Having mapped the six major transition pathways in $NaYF_4$:Er^{3+}/Tm^{3+} and their relationships, we can devise a generalized scheme (Scheme 2) to program spectrally pure emission in other materials. In this scheme, a "router" state receives the energy absorbed from photons and directs it through an energy concentration pathway to a storage state, which participates in an ETU pathway with the router state to populate the emitting state. The emitter can then release its energy as photons or recycle the energy back to the router or storage states.

Scheme 2. Generalized Scheme for Spectrally Pure Upconverted Emission in Lanthanide-Doped Materials

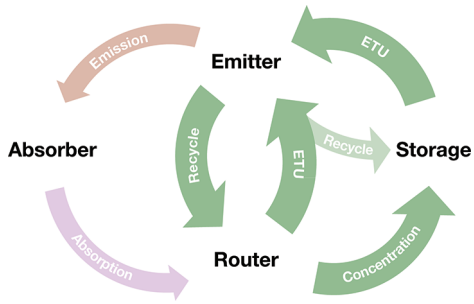

We anticipate being able to use our high-throughput in silico screening method to predict more multiply doped combinations that participate in this generalized scheme, and we expect that our pathway analysis algorithm can elucidate more mechanisms giving rise to spectrally pure emission or other desirable properties. Ultimately, the ability to induce spectrally pure emission in upconverting nanoparticles will enable multiplexed tracking of single particles and biological species in diverse media, as well as many other applications that require strong and precisely defined optical transitions.

■ ASSOCIATED CONTENT

Supporting Information

Spectroscopic data, simulation parameters, major Er^{3+} transitions, and absolute quantum yield measurement procedures. This material is available free of charge via the Internet at http://pubs.acs.org.

■ AUTHOR INFORMATION

Corresponding Author

*E-mail: emchan@lbl.gov.

Notes

The authors declare no competing financial interest.

■ ACKNOWLEDGMENTS

The authors thank Rashid Zia and Christopher Dodson, who provided invaluable assistance with calculations, and thank Gang Han and Alexis Ostrowski for assistance with synthetic techniques. D.J.M. was supported by a DOE Early Career Research Program award. This work was carried out entirely at the Molecular Foundry and was supported by the Office of Science, Office of Basic Energy Sciences, of the U.S. Department of Energy under Contract No. DE-AC02-05CH11231.

■ REFERENCES

(1) Miller, J. N. *Analyst* **2005**, *130*, 265−270.
(2) Stryer, L.; Haugland, R. *Proc. Natl. Acad. Sci. U.S.A.* **1967**, *58*, 719−726.
(3) Ju, J.; Ruan, C.; Fuller, C. W.; Glazer, A. N.; Mathies, R. A. *Proc. Natl. Acad. Sci. U.S.A.* **1995**, *92*, 4347−4351.
(4) Auzel, F. *J. Lumin.* **1990**, *45*, 341−345.
(5) Wang, F.; Banerjee, D.; Liu, Y.; Chen, X.; Liu, X. *Analyst* **2010**, *135*, 1839−1854.
(6) Wang, F.; Liu, X. *Chem. Soc. Rev.* **2009**, *38*, 976−989.
(7) Vennerberg, D.; Lin, Z. *Sci. Adv. Mater.* **2011**, *3*, 26−40.
(8) Heer, S.; Kompe, K.; Gudel, H.; Haase, M. *Adv. Mater.* **2004**, *16*, 2102−2105.
(9) Wu, S.; Han, G.; Milliron, D. J.; Aloni, S.; Altoe, V.; Talapin, D. V.; Cohen, B. E.; Schuck, P. J. *Proc. Natl. Acad. Sci. U.S.A.* **2009**, *106*, 10917−10921.
(10) Ostrowski, A. D.; Chan, E. M.; Gargas, D. J.; Katz, E. M.; Han, G.; Schuck, P. J.; Milliron, D. J.; Cohen, B. E. *ACS Nano* **2012**, *6*, 2686−2692.
(11) Nam, S. H.; Bae, Y. M.; Park, Y. I.; Kim, J. H.; Kim, H. M.; Choi, J. S.; Lee, K. T.; Hyeon, T.; Suh, Y. D. *Angew. Chem., Int. Ed.* **2011**, *50*, 6093−6097.
(12) Shan, J.; Chen, J.; Meng, J.; Collins, J.; Soboyejo, W.; Friedberg, J. S.; Ju, Y. *J. Appl. Phys.* **2008**, *104*, 094308.
(13) Suijver, J. F. In *Luminescence: From Theory to Applications*; Ronda, C., Ed.; Wiley-VCH: Weinheim, 2008; pp 133−178.
(14) Patra, A.; Friend, C. S.; Kapoor, R.; Prasad, P. N. *J. Phys. Chem. C* **2002**, *106*, 1909−1912.
(15) Lim, S. F.; Riehn, R.; Ryu, W. S.; Khanarian, N.; Tung, C.; Tank, D.; Austin, R. H. *Nano Lett.* **2006**, *6*, 169−174.
(16) Xiong, L.-Q.; Chen, Z.-G.; Yu, M.-X.; Li, F.-Y.; Liu, C.; Huang, C.-H. *Biomaterials* **2009**, *30*, 5592−5600.
(17) Carnall, W. T.; Goodman, G. L.; Rajnak, K.; Rana, R. S. *J. Chem. Phys.* **1989**, *90*, 3443−3457.
(18) Dejneka, M. J.; Streltsov, A.; Pal, S.; Frutos, A. G.; Powell, C. L.; Yost, K.; Yuen, P. K.; Müller, U.; Lahiri, J. *Proc. Natl. Acad. Sci. U.S.A.* **2003**, *100*, 389−393.
(19) Zhang, F.; Haushalter, R. C.; Haushalter, R. W.; Shi, Y.; Zhang, Y.; Ding, K.; Zhao, D.; Stucky, G. D. *Small* **2011**, *7*, 1972−1976.
(20) Niu, W.; Wu, S.; Zhang, S. *J. Mater. Chem.* **2010**, *20*, 9113.
(21) Niu, W.; Wu, S.; Zhang, S.; Li, J.; Li, L. *Dalton Trans.* **2011**, *40*, 3305−3314.
(22) Chen, G.; Liu, H.; Somesfalean, G.; Liang, H.; Zhang, Z. *Nanotechnology* **2009**, *20*, 385704.
(23) Wang, G.; Peng, Q.; Li, Y. *Chem.—Eur. J.* **2010**, *16*, 4923−4931.
(24) Zou, X. L.; Shikida, A.; Yanagita, H.; Toratani, H. *J. Non-Cryst. Solids* **1995**, *181*, 100−109.
(25) Shen, X.; Nie, Q.; Xu, T.; Peng, T.; Gao, Y. *Phys. Lett. A* **2004**, *332*, 101−106.
(26) de Souza, A. B.; de Araujo, M. T.; Vermelho, M. V. D.; Cassanjes, F. C.; Ribeiro, S. J. L.; Massaddeq, Y. *J. Non-Cryst. Solids* **2007**, *353*, 94−101.
(27) Chen, D.; Wang, Y.; Bao, F.; Yu, Y. *J. Appl. Phys.* **2007**, *101*, 113511.
(28) Alivisatos, A. P. *Science* **1996**, *271*, 933−937.
(29) Walsh, B.; Barnes, N.; Di Bartolo, B. *J. Appl. Phys.* **1998**, *83*, 2772−2787.
(30) Karaveli, S.; Zia, R. *Phys. Rev. Lett.* **2011**, 106.
(31) van Dijk, J. M. F.; Schuurmans, M. F. H. *J. Chem. Phys.* **1983**, *78*, 5317−5323.
(32) Miyakawa, T.; Dexter, D. *Phys. Rev. B* **1970**, *1*, 2961−2969.

(33) Kushida, T. *J. Phys. Soc. Jpn.* **1973**, *34*, 1318−1326.
(34) Di Bartolo, B. *Energy Transfer Processes in Condensed Matter; NATO Advanced Studies Institute*; Plenum Press: New York, 1983; p 156.
(35) Judd, B. R. *Phys. Rev.* **1962**, *127*, 750−761.
(36) Ofelt, G. S. *J. Chem. Phys.* **1962**, *37*, 511−520.
(37) Riseberg, L. A.; Moos, H. W. *Phys. Rev.* **1968**, *174*, 429−438.
(38) Song, F.; Zhang, K.; Su, J.; Han, L.; Liang, J.; Zhang, X.; Yan, L.; Tian, J.; Xu, J. *Opt. Express* **2006**, *14*, 12584−12589.
(39) Thomas, D. D.; Carlsen, W. F.; Stryer, L. *Proc. Natl. Acad. Sci. U.S.A.* **1978**, *75*, 5746−5750.
(40) Ivanova, S. E.; Tkachuk, A. M.; Mirzaeva, A.; Pelle, F. *Opt. Spectrosc.* **2008**, *105*, 228−241.
(41) Kaminskii, A. A. *Crystalline Lasers; physical processes and operating schemes*; CRC Press: Boca Raton, FL, 1996.
(42) Suyver, J.; Grimm, J.; van Veen, M.; Biner, D.; Kramer, K.; Gudel, H. *J. Lumin.* **2006**, *117*, 1−12.
(43) Mai, H.-X.; Zhang, Y.-W.; Sun, L.-D.; Yah, C.-H. *J. Phys. Chem. C* **2007**, *111*, 13721−13729.
(44) Chan, E. M.; Xu, C.; Mao, A. W.; Han, G.; Owen, J. S.; Cohen, B. E.; Milliron, D. J. *Nano Lett.* **2010**, *10*, 1874−1885.
(45) Roberts, J. E. *J. Am. Chem. Soc.* **1961**, *83*, 1087−1088.